

Correspondence between real-space topology and spectral flows at disclinationsBoyang Xie,¹ Weiyin Deng,² Jiuyang Lu,² Hui Liu,¹ Pengtao Lai,¹ Hua Cheng,^{1,*}
Zhengyou Liu,^{2,3,*} and Shuqi Chen^{1,4,*}¹*The Key Laboratory of Weak Light Nonlinear Photonics, Ministry of Education, Smart Sensing Interdisciplinary Science Center,
School of Physics and TEDA Institute of Applied Physics, Nankai University, Tianjin 300071, China*²*Key Laboratory of Artificial Micro- and Nanostructures of Ministry of Education and School of Physics and Technology,
Wuhan University, Wuhan 430072, China*³*Institute for Advanced Studies, Wuhan University, Wuhan 430072, China*⁴*The Collaborative Innovation Center of Extreme Optics, Shanxi University, Taiyuan, Shanxi 030006, China*

(Received 20 June 2023; revised 10 October 2023; accepted 11 October 2023; published 27 October 2023)

The recent interest in topological states localized to disclinations has highlighted the bulk-disclination correspondence, which links the reciprocal-space topology of a lattice to the emergence of such states. In this work, we extend such correspondence to the real-space topology. We construct a lattice with trivial reciprocal-space topology, in which the emergence of topological states and spectral flows at disclinations is induced by real-space topology. We experimentally verify the correspondence between real-space topology and disclination states in electrical circuit systems. Our findings offer insight into the real-space topology and enrich the family of topological states with their realization in topoelectrical circuits.

DOI: [10.1103/PhysRevB.108.134118](https://doi.org/10.1103/PhysRevB.108.134118)**I. INTRODUCTION**

In recent years, topological defects that reflect the bulk and real-space topology have become a topic of great interest in the field of topological physics. These defects include dislocations [1,2], vortex distortions [3–5], and disclinations [6–10]. Disclinations, which are defects of rotational symmetry, can trap fractional charges induced by higher-order topology and form localized bound states [11–14]. The phenomenon of topological disclination states is explained by the bulk-disclination correspondence [12], which links the reciprocal-space topology of the lattice to their emergence. However, this correspondence is not always sufficient, as shown by recent discoveries of symmetry-protected disclination states in the absence of reciprocal-space topology [15,16]. In these cases, the interplay between localized orbitals and Bloch wave functions becomes more essential for topological effects at disclinations, revealing that the real-space topology also plays an important role in addition to the reciprocal-space topology of the bulk.

The real-space topology and the related orbital-induced phenomena can be described by the framework of topological quantum chemistry, which offers a new way to characterize the band theory of materials by combining descriptions in real and reciprocal space [17–20]. Higher-order topological insulators [21,22] and fragile topological insulators [23,24] that go beyond the traditional bulk-boundary correspondence have been uniformly depicted in this framework. In these materials, the gapped bands can always be expressed as a combination

of elementary band representations that originate from atomic orbitals at Wyckoff positions, i.e., high-symmetry points in real space. The real-space invariants (RSIs) attributed to such a combination give rise to spectral flows under twisted boundary conditions [25]. Spectral flows have been observed in fragile topological systems [26] and obstructed atomic limit (OAL) topological phases [27].

In this work, by exploring spectral flows at disclinations, we extend the bulk-disclination correspondence to the real-space topology. We demonstrate that the disclination states induced by the localized orbitals can contribute to the gapless spectral flows. We first construct a tight-binding lattice possessing nonzero RSIs and a trivial topological index in reciprocal space and find that spectral flows emerge at disclinations with Frank angles of $\pi/3$, $2\pi/3$, and π . Then we observe the spectral signatures and symmetry properties of topological disclination states in topoelectrical circuits. Owing to the one-to-one mapping to the lattice model and high manipulability, electrical circuits provide an ideal platform for controlling the hopping parameter in a distorted lattice [28–32]. All theoretical, numerical, and experimental results consistently evidence the correspondence between the real-space topology and spectral flows at disclinations.

II. MODEL AND METHODS

We first consider a tight-binding model in the wallpaper group $p6mm$ (C_{6v}) before introducing disclinations. The unit cell of the lattice is shown in Fig. 1(a), with the intracell and extracell couplings t_1 and t_2 , respectively, each having negative values. By varying t_1 and t_2 , we observe two OAL phases with distinct topological properties, where the Wannier charge centers are located at Wyckoff position $1a$ or $3c$, away from

*Corresponding authors: hcheng@nankai.edu.cn;
zylui@whu.edu.cn; schen@nankai.edu.cn

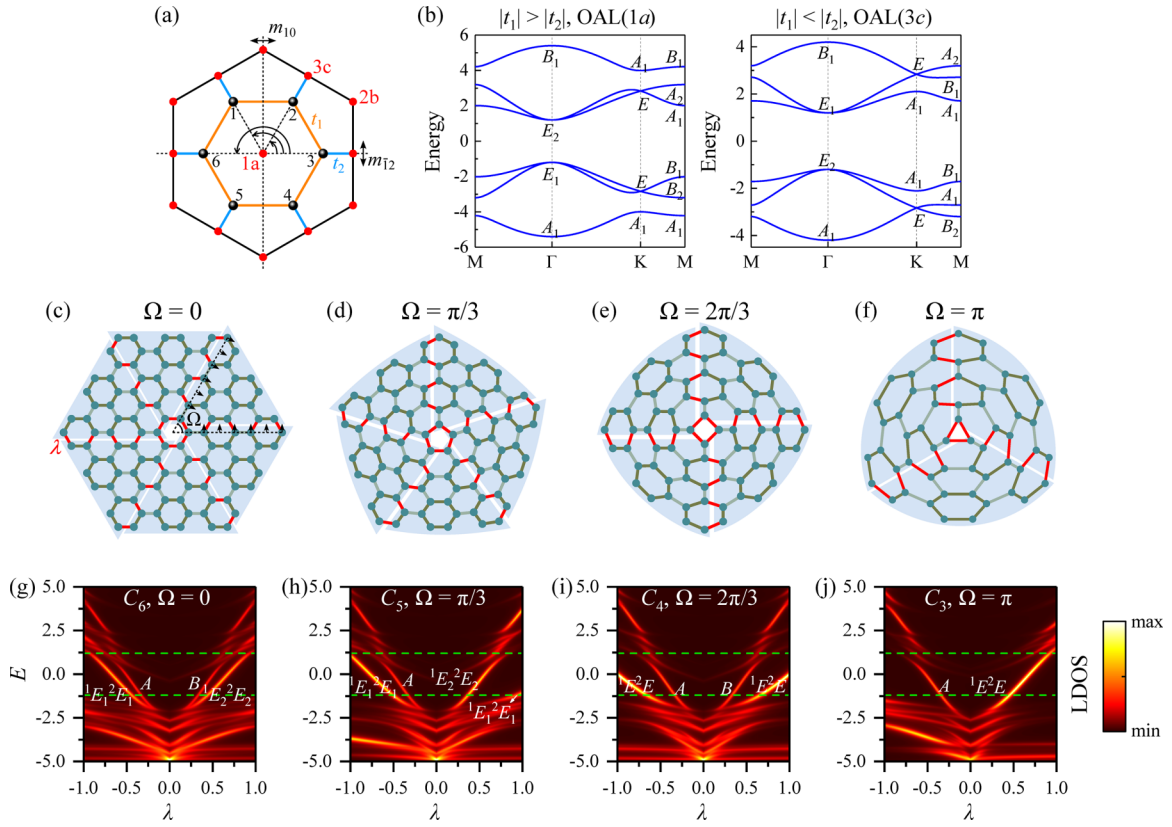


FIG. 1. Tight-binding model for introducing disclination and spectral flows. (a) Unit cell with Kekulé modulation of the coupling. The lattice sites are denoted as black spheres. The labels of the Wyckoff positions are in red. The couplings within unit cells (orange lines) and among neighboring unit cells (blue lines) are represented by t_1 and t_2 , respectively. (b) Band structures of the tight-binding model for the OAL(1a) phase with $|t_1| > |t_2|$ and the OAL(3c) phase with $|t_1| < |t_2|$. Little-group representations are labeled for each band. (c) Schematic of the tight-binding model with a hexagonal lattice. (d)–(f) Tight-binding models in which disclinations with Frank angles of $\pi/3$, $2\pi/3$, and π are introduced, causing the lattice to become C_5 , C_4 , and C_3 symmetric, respectively. (g)–(j) Topological states and spectral flows as a function of the hopping multiplication factor λ . The lattices are C_6 , C_5 , C_4 , and C_3 symmetric, respectively. The bulk band gap at $\lambda = 1$ is between the green dashed lines.

the lattice sites [33]. The band structures for the OAL(1a) phase ($|t_1| > |t_2|$) and OAL(3c) phase ($|t_1| < |t_2|$) are displayed in Fig. 1(b). Through an analysis of the irreducible representations (irreps) of the three lower bands, we determine that the decompositions of elementary band representations for the OAL(1a) and OAL(3c) phases are $(A_1)_{1a} \oplus (E_1)_{1a}$ and $(A_1)_{3c}$, respectively. While the OAL(3c) phase has a nontrivial bulk polarization, the OAL(1a) phase has a trivial topological index in reciprocal space [6,34]. A more detailed explanation of this deduction from the perspective of topological quantum chemistry is provided in Appendix A 1.

In order to probe the real-space topology, a C_n -symmetric twisted boundary condition that passes through the symmetry center of the system is introduced. We present a C_6 -symmetric twisted boundary condition in Fig. 1(c) which divides the system into six parts that transform into each other under C_6 . The hopping strength across the cut is multiplied by λ , and to ensure a well-defined gauge transformation, the cut cannot pass through sites, only through couplings. For sites near the twisted boundary, the on-site energy is a function of nearest-neighbor hopping and is given by $2t_1 + t_2 + \sum |t_{NN}|$. It is important to note that the shift in the on-site energy does

not close the band gap or alter the topological characteristics of the spectral flows.

The existence of gapless spectral flow depends on the real-space topology of Wannier orbitals at Wyckoff positions. RSIs with time-reversal symmetry determine the imbalance of the C_n -symmetric eigenstates below the band gap and are functions of irrep multiplicities, as given by [25]

$$\begin{aligned} \delta_1 &= -m(A) + m({}^1E_1^2E_1), \\ \delta_2 &= -m(A) + m({}^1E_2^2E_2), \\ \delta_3 &= -m(A) + m(B). \end{aligned} \quad (1)$$

The nonzero RSIs for the OAL(1a) and OAL(3c) phases are $(\delta_1, \delta_2, \delta_3)_{1a} = (0, -1, -1)$ and $\delta_{3c} = -1$, respectively. For $\lambda = \pm 1$, crossing the C_n -symmetric twisted boundary is equivalent to a gauge transformation for the system's Hamiltonian, given by

$$H(\lambda) = V(\lambda)H(1)V^\dagger(\lambda). \quad (2)$$

If $|\psi\rangle$ is an eigenstate of $H(1)$ with C_n eigenvalue ξ , $V(\lambda)|\psi\rangle$ is an eigenstate of $H(\lambda)$ with C_n eigenvalue $\lambda\xi$. The gauge transformation under $\lambda = -1$ interchanges irreps ${}^1E_1^2E_1$ with

${}^1E_2^2E_2$ and A with B , while the multiplicities below the band gap are changed to $\delta_1 - \delta_2$ and δ_3 .

The spectral flows arising from nonzero RSIs are characterized by two pairs of level crossings: one pair with irreps ${}^1E_1^2E_1$ and ${}^1E_2^2E_2$ and another with irreps A and B . To observe the spectral flows, we can examine the local density of states at the central cell along the path $(\lambda = 1) \rightarrow (\lambda = -1)$, as shown in Fig. 1(g). The spectrum at λ and $-\lambda$ is symmetric under C_2 due to the gauge transformation $H(-\lambda) = VH(\lambda)V^\dagger$. However, in contrast to the OAL(1a) phase, the spectral flows vanish in the OAL(3c) phase because the RSIs are trivial at Wyckoff position 1a. Instead, the orbital $(A_1)_{3c}$ gives rise to spectral flows in the OAL(3c) phase under C_2 -symmetric twisted boundary conditions. More details can be found in Appendix A. It is also worth noting that the corner states due to bulk polarization in the OAL(3c) phase do not contribute to the topological spectral flows (see Fig. 5 in Appendix A). This is attributed to the trivial real-space invariants $(\delta_1, \delta_2)_{1a} = (0, 0)$ for the OAL(3c) phase, whose corner states do not induce any imbalance in the multiplicities of states within the bulk band.

We utilized the Volterra process to introduce disclinations into the honeycomb lattice by removing a section from the lattice structure [13]. With this method, we generated C_5 -, C_4 -, and C_3 -symmetric structures with Frank angles of $\Omega = \pi/3$, $2\pi/3$, and π , respectively, as illustrated in Figs. 1(d)–1(f). The local density of states in Figs. 1(h)–1(j) demonstrates the observation of topological states and spectral flows in these structures. Specifically, each irrep in the rotation group C_n appears in the band gap. Disclination states with irreps ${}^1E_1^2E_1$, ${}^1E^2E$, and ${}^1E^2E$ appear in C_5 -, C_4 -, and C_3 -symmetric structures near $\lambda = \pm 1$, respectively. The eigenvalues of the rotation operator of these states are $e^{\pm 2\pi/n}$, indicating an angular momentum of $l = \pm 1$. These disclination states do not contribute to robust gapless spectral flows. On the other hand, other irreps with $l \neq \pm 1$ form gapless spectral flows, which remain robust against the shifting of on-site energy, as demonstrated in Fig. 6 in Appendix A 2. In C_4 -symmetric lattices, the spectrum at λ and $-\lambda$ is symmetric due to the gauge transformation under C_2 , as shown in Fig. 1(i). However, twisted boundaries lacking C_2 symmetry with $\lambda = -1$ under C_5 or C_3 do not support gauge transformations due to geometric frustration. In such cases, the eigenstates of $H(1)$ and $H(-1)$ are inverted, with the eigenvalues shifted from E to $-E$. This inversion of states results in asymmetric spectral flows in lattices under C_5 or C_3 , as demonstrated in Figs. 1(h) and 1(j).

The Wannier orbitals remain localized at the unit cell centers even under disclination and produce the topological states at the disclination core. Among these states, irrep A originating from the $(A_1)_{1a}$ orbital causes an imbalance in the bulk states below the band gap. The corresponding RSIs for the C_5 -symmetric lattice can be defined as

$$\begin{aligned}\delta_1 &= -m(A) + m({}^1E_1^2E_1), \\ \delta_2 &= -m(A) + m({}^1E_2^2E_2).\end{aligned}\quad (3)$$

In the OAL(1a) and OAL(3c) phases, the RSIs are $(\delta_1, \delta_2)_{1a} = (-1, -1)$ and $(\delta_1, \delta_2)_{1a} = (0, 0)$, respectively. While disclination states with irreps ${}^1E_1^2E_1$ do not contribute to band closing under the twisted boundary, the nonzero RSIs lead to

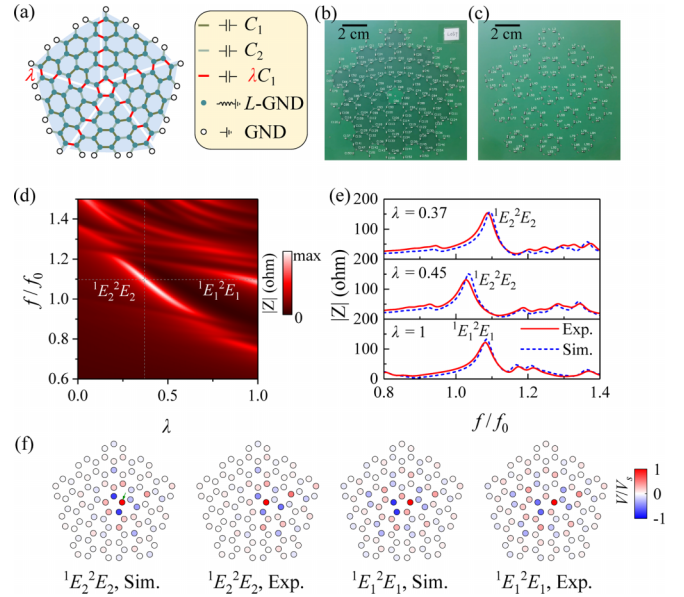


FIG. 2. Experiment measuring a C_5 -symmetric topoelectrical circuit. (a) Circuit model of the C_5 -symmetric lattice. (b) and (c) Top and bottom layers of the double-sided printed circuit board. (d) Simulated impedance between the ground and center nodes. (e) Experiment and simulation results of the impedance spectrum at $\lambda = 0.37, 0.45$, and 1 . (f) Simulated and experimental results of the voltage distribution at the resonance frequency of ${}^1E_2^2E_2$ and ${}^1E_1^2E_1$ states. A voltage source with an amplitude of V_0 is applied between a node at the disclination core (green arrow) and the ground.

topological spectral flows of states with irreps A and ${}^1E_2^2E_2$, flowing from the lower bands to the upper bands and from the upper bands to the lower bands, respectively. In contrast, no disclination states or spectral flows are observed at the lattice center in the OAL(3c) phase (see Fig. 5 in Appendix A 1). Similar properties are found in C_4 - and C_3 -symmetric structures, where the RSIs are nonzero in the OAL(1a) phase.

In C_4 -symmetric lattices, a twisted boundary with $\lambda = -1$ is equivalent to a gauge transformation that transforms irrep A into irrep B , causing a state with irrep B to flow from the upper bands to the lower bands, as observed in Fig. 1(i). Disclination states with irreps ${}^1E^2E$ were experimentally demonstrated earlier in an acoustic system [15] for the OAL(1a) phase with C_4 symmetry and $\lambda = 1$. Compared to the results considering only the bulk-disclination correspondence [12], the divergence in the OAL(1a) phase arises due to the Wannier orbitals at the disclination core. Removing atoms from the core cell leads to the disappearance of the disclination states and spectral flows in the OAL(1a) phase, while the RSIs become trivial. Moreover, in the OAL(3c) phase, the separation of the charge associated with the Wannier center at Wyckoff position 3c leads to the appearance of higher-order states at the inner corner, as demonstrated in Fig. 7 in Appendix A 2.

III. EXPERIMENT REALIZATION IN TOPOELECTRICAL CIRCUITS

To establish the one-to-one mapping to the tight-binding model, we conducted our experiment using electrical circuits (see Appendix B for details). Figure 2(a) shows the schematic

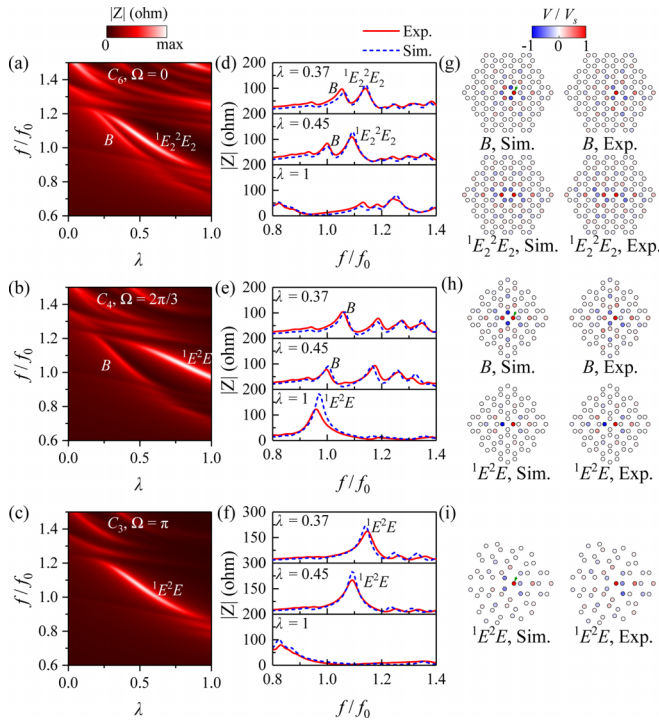


FIG. 3. Impedance spectrum and voltage distribution in C_6 -, C_4 -, and C_3 -symmetric circuits. (a)–(c) Simulated impedance between the ground and the center node. The circuits are (a) C_6 , (b) C_4 , and (c) C_3 symmetric with Frank angles of 0 , $2\pi/3$, and π , respectively. The irreps are labeled for the spectral flows. (d)–(f) Experiment and simulation results of the impedance spectrum at $\lambda = 0.37$, 0.45 , and 1 . (g)–(i) Simulated (left) and experimental (right) results of the voltage distribution at the resonance frequency. A voltage source with an amplitude of V_0 is applied between a node at the disclination core (green arrow) and the ground.

of a circuit with a C_5 -symmetric lattice which was realized on a two-layer printed circuit board. The capacitors or inductors are placed on the top or bottom layer, as shown in Figs. 2(b) and 2(c), with the couplings controlled by the capacitors between the nodes. In Fig. 2(d), we present the impedance spectrum obtained by simulating C_5 -symmetric circuits using COMSOL MULTIPHYSICS, where the impedance bands in electrical circuits appear upside down compared to those in the tight-binding model. The correspondence between the impedance bands and the eigenvalue of $J(\lambda, \omega)$ is given in Fig. 9 in Appendix B. The measured impedance spectra between a node in the core and the ground are shown in Fig. 2(e), along with the simulation results. The experimental data show great agreement with the simulation results. To visualize the eigenstates, we stimulated them by inputting the voltage signal at peak frequencies into one node in the core (green arrow). The simulated and measured voltage field distributions are shown in Fig. 2(f), and they match the symmetries of the corresponding irreps, confirming the appearance of topological states and spectral flow of irreps ${}^1E_2 {}^2E_2$ at disclination. Although the circuit model here supports only positive λ with the basic modes, it is possible to achieve negative λ in p -orbital bands in more complex circuit models (Fig. 10 in Appendix B).

Figure 3 presents the simulated [Figs. 3(a)–3(c)] and experimental [Figs. 3(d)–3(f)] results of impedance and voltage measurements [Figs. 3(g)–3(i)] in topoelectrical circuits with C_6 , C_4 , and C_3 symmetries. The measured impedance spectra at $\lambda = 0.37$ and $\lambda = 0.45$ reveal the presence of spectral flows, which is further confirmed by examining the field distribution at the peak frequency. In the C_6 -symmetric circuit, two spectral flows of irreps B and ${}^1E_2 {}^2E_2$ are observed, characterized by odd and even field distributions under C_2 , respectively. The C_4 -symmetric circuit features a spectral flow of irrep B with even field distribution under C_2 and disclination states of irreps ${}^1E_1 {}^2E_1$ that exhibit chiral symmetry at $\lambda = 1$ but disappear into the bulk as λ decreases. The C_3 -symmetric circuit is characterized by disclination states of irreps ${}^1E^2E$ in the band gap. These experimental results confirm the theoretical model in Fig. 1 and provide a comprehensive understanding of topological states and spectral flows in Wannierizable systems with disclinations.

IV. CONCLUSIONS

In conclusion, we successfully demonstrated the existence of topological states and spectral flows at disclinations of OAL phases. Our results, manifested by topoelectrical circuits, provide insight into the real-space topology and spectral signatures of disclination states. The introduced twisted boundaries serve as a probe for detecting orbitals at Wyckoff positions and further provide an approach for controlling localized states at disclinations. In addition, the relation between the real-space topology and disclination states can be explored in three- or fractional-dimensional systems, which may exhibit intriguing properties of spectral flows.

The spectral flow could also potentially occur through the implementation of Kekulé modulation, which involves polar parameters. Consequently, the spectral flow of corner states may merge into a vortex defect state, leading to the emergence of Majorana-like zero modes [35]. In our study, we created lattice defects through disclination, which does not involve polar parameters. Moreover, the bound states do not originate from corner states due to the trivial topology of reciprocal space. The disclination states were ensured by lattice symmetry and characterized by real-space topology.

ACKNOWLEDGMENTS

This work was supported by the National Key Research and Development Program of China (Grants No. 2022YFA1404501, No. 2022YFA1404900, and No. 2021YFA1400601), the National Natural Science Fund for Distinguished Young Scholar (Grant No. 11925403), the National Natural Science Foundation of China (Grants No. 12122406, No. 12192253, No. 12004198, and No. 12304486), and the China Postdoctoral Science Foundation (Grant No. 2020M680850).

APPENDIX A: TIGHT-BINDING MODEL AND ROBUSTNESS OF SPECTRAL FLOWS

1. Real-space invariants as indicators of spectral flows

We introduce a tight-binding model for a honeycomb lattice with Kekulé modulation. The primitive lattice vectors are

$a_1 = (a, 0)$ and $a_2 = (a/2, \sqrt{3}a/2)$, where we set $a = 1$ in the following. The basis is referred to the wave functions of sites

$$H = \begin{pmatrix} 0 & t_1 & 0 \\ t_1 & 0 & t_1 \\ 0 & t_1 & 0 \\ t_2 e^{i(-k_x/2 + \sqrt{3}k_y/2)} & 0 & t_1 \\ 0 & t_2 e^{i(k_x/2 + \sqrt{3}k_y/2)} & 0 \\ t_1 & 0 & t_2 e^{ik_x} \end{pmatrix}$$

where t_1 and t_2 are intracell and extracell couplings and k_x and k_y are components of Bloch wave vector \mathbf{k} . Here, t_1 and t_2 are negative. The band structures of two topologically distinct phases with $|t_1| > |t_2|$ and $|t_1| < |t_2|$ are presented in Figs. 1(b) and 1(c) in the main text. The corresponding irreducible representations for the high-symmetry points of the Brillouin zone are provided in Table I. The topology of a gapped band structure is characterized by the symmetry data vector B , which is a linear combination of elementary band representations (EBRs),

$$B = \sum_i p_i \text{EBR}_i. \quad (\text{A2})$$

TABLE I. Character tables for the point group of $p6mm$ and its relevant little groups. The first column gives the standard name (SN) of representation (Rep) according to Altmann-Herzig notation [36], and the second column gives the name at the high-symmetry points (HSP) in the Brillouin zone.

C_{6v} ($6mm$), Γ point							
Rep		E	c_6	c_3	c_2	$m_{\bar{1}2}$	m_{10}
SN	HSP						
A_1	Γ_1	1	1	1	1	1	1
A_2	Γ_2	1	1	1	1	-1	-1
B_2	Γ_4	1	-1	1	-1	-1	1
B_1	Γ_3	1	-1	1	-1	1	-1
E_1	Γ_6	2	-1	-1	-2	0	0
E_2	Γ_5	2	1	-1	2	0	0

C_{3v} ($3m$), little group for the K point					
Rep		E	c_3	$m_{\bar{1}2}$	m_{10}
SN	HSP				
A_1	K_1	1	1	1	
A_2	K_2	1	1	-1	
E	K_3	2	-1	1	

C_{2v} ($2mm$), little group for the M point					
Rep		E	c_2	$m_{\bar{1}2}$	m_{10}
SN	HSP				
A_1	M_1	1	1	1	1
A_2	M_2	1	1	-1	-1
B_1	M_3	1	-1	1	-1
B_2	M_4	1	-1	-1	1

1 to 6 in Fig. 1(a). The Bloch Hamiltonian considering the nearest-neighbor hopping is

$$H = \begin{pmatrix} t_2 e^{i(k_x/2 - \sqrt{3}k_y/2)} & 0 & t_1 \\ 0 & t_2 e^{-i(k_x/2 + \sqrt{3}k_y/2)} & 0 \\ t_1 & 0 & t_2 e^{-ik_x} \\ 0 & t_1 & 0 \\ t_1 & 0 & t_1 \\ 0 & t_1 & 0 \end{pmatrix}, \quad (\text{A1})$$

A complete list of the spinless EBRs for $p6mm$ with time-reversal symmetry and without spin-orbit coupling is presented in Table II. The decomposition of the three lower bands according to Table II are

$$\begin{aligned} (A_1)_{1a} \oplus (E_1)_{1a} & \text{ for } |t_1| > |t_2|, \\ (A_1)_{3c} & \text{ for } |t_1| < |t_2|. \end{aligned} \quad (\text{A3})$$

The integer decomposition for $|t_1| > |t_2|$ corresponds to Wyckoff position $1a$, while the integer decomposition for $|t_1| < |t_2|$ corresponds to Wyckoff position $3c$. The EBRs indicate the presence of two obstructed atomic limit (OAL) topological phases, where the Wannier charge centers are located away from the lattice sites. The nontrivial real-space invariants (RSIs) determining the imbalance in multiplicities of irreps are $(\delta_1, \delta_2, \delta_3)_{1a} = (0, -1, -1)$ for $|t_1| > |t_2|$ and $\delta_{3c} = -1$ for $|t_1| < |t_2|$.

Following the character tables of rotation groups C_n presented in Table III, we determine the RSIs under twisted boundaries. The location of orbitals at different Wyckoff positions can be probed by introducing the C_2 twisted boundary. When the C_2 twisted boundary is introduced into the C_{6v} system, the irreps of C_{6v} can be reduced to C_2 as

$$\begin{aligned} A_1 \downarrow 2 &= A, & A_2 \downarrow 2 &= A, & B_1 \downarrow 2 &= B, \\ B_2 \downarrow 2 &= B, & E_1 \downarrow 2 &= 2B, & E_2 \downarrow 2 &= 2A. \end{aligned} \quad (\text{A4})$$

TABLE II. Elementary band representations (EBRs) for $p6mm$. The first column denotes the EBR as $(R)_l$. R is the irreducible representation of the orbital that induced the EBR. l denotes the maximal Wyckoff position where the orbital is located.

EBR	Γ	K	M
$(A_1)_{1a}$	Γ_1	K_1	M_1
$(A_2)_{1a}$	Γ_2	K_2	M_2
$(B_1)_{1a}$	Γ_4	K_2	M_4
$(B_2)_{1a}$	Γ_3	K_1	M_3
$(E_1)_{1a}$	Γ_6	K_3	$M_3 \oplus M_4$
$(E_2)_{1a}$	Γ_5	K_3	$M_1 \oplus M_2$
$(A_1)_{2b}$	$\Gamma_1 \oplus \Gamma_4$	K_3	$M_1 \oplus M_4$
$(A_2)_{2b}$	$\Gamma_2 \oplus \Gamma_3$	K_3	$M_2 \oplus M_3$
$(E)_{2b}$	$\Gamma_5 \oplus \Gamma_6$	$K_1 \oplus K_2 \oplus K_3$	$M_1 \oplus M_2 \oplus M_3 \oplus M_4$
$(A_1)_{3c}$	$\Gamma_1 \oplus \Gamma_5$	$K_1 \oplus K_3$	$M_1 \oplus M_3 \oplus M_4$
$(A_2)_{3c}$	$\Gamma_2 \oplus \Gamma_5$	$K_2 \oplus K_3$	$M_2 \oplus M_3 \oplus M_4$
$(B_1)_{3c}$	$\Gamma_3 \oplus \Gamma_6$	$K_1 \oplus K_3$	$M_1 \oplus M_2 \oplus M_3$
$(B_2)_{3c}$	$\Gamma_4 \oplus \Gamma_6$	$K_2 \oplus K_3$	$M_1 \oplus M_2 \oplus M_4$

TABLE III. Character tables of rotation groups for twisted boundaries. In each table, symbols in the first column use Altmann-Herzig notation.

		C_2				
Rep	1	2				
A	1	1				
B	1	-1				
		C_3				
Rep	1	3^+	3^-			
A	1	1	1			
2E	1	$e^{i\frac{2\pi}{3}}$	$e^{-i\frac{2\pi}{3}}$			
1E	1	$e^{-i\frac{2\pi}{3}}$	$e^{i\frac{2\pi}{3}}$			
		C_4				
Rep	1	4^+	2	4^-		
A	1	1	1	1		
B	1	-1	1	-1		
1E	1	$-i$	-1	i		
2E	1	i	-1	$-i$		
		C_5				
Rep	1	5^+	$(5^+)^2$	$(5^-)^2$	5^-	
A	1	1	1	1	1	
1E_1	1	$e^{-i\frac{2\pi}{5}}$	$e^{-i\frac{4\pi}{5}}$	$e^{i\frac{4\pi}{5}}$	$e^{i\frac{2\pi}{5}}$	
2E_1	1	$e^{i\frac{2\pi}{5}}$	$e^{i\frac{4\pi}{5}}$	$e^{-i\frac{4\pi}{5}}$	$e^{-i\frac{2\pi}{5}}$	
1E_2	1	$e^{-i\frac{4\pi}{5}}$	$e^{i\frac{2\pi}{5}}$	$e^{-i\frac{2\pi}{5}}$	$e^{i\frac{4\pi}{5}}$	
2E_2	1	$e^{i\frac{4\pi}{5}}$	$e^{-i\frac{2\pi}{5}}$	$e^{i\frac{2\pi}{5}}$	$e^{-i\frac{4\pi}{5}}$	
		C_6				
Rep	1	6^+	3^+	2	3^-	6^-
A	1	1	1	1	1	1
B	1	-1	1	-1	1	-1
1E_1	1	$e^{-i\frac{\pi}{3}}$	$e^{-i\frac{2\pi}{3}}$	-1	$e^{i\frac{2\pi}{3}}$	$e^{i\frac{\pi}{3}}$
2E_1	1	$e^{i\frac{\pi}{3}}$	$e^{i\frac{2\pi}{3}}$	-1	$e^{-i\frac{2\pi}{3}}$	$e^{-i\frac{\pi}{3}}$
1E_2	1	$e^{i\frac{2\pi}{3}}$	$e^{i\frac{4\pi}{3}}$	1	$e^{i\frac{2\pi}{3}}$	$e^{i\frac{4\pi}{3}}$
1E_2	1	$e^{-i\frac{2\pi}{3}}$	$e^{-i\frac{4\pi}{3}}$	1	$e^{-i\frac{2\pi}{3}}$	$e^{-i\frac{4\pi}{3}}$

The reduced RSIs with a C_2 twisted boundary are

$$\begin{aligned} \delta'_{1a} = 1, \quad \delta'_{3c} = 0 & \quad \text{for } |t_1| > |t_2|, \\ \delta'_{1a} = 0, \quad \delta'_{3c} = -1 & \quad \text{for } |t_1| < |t_2|, \end{aligned} \quad (\text{A5})$$

where $\delta' = -m(A) + m(B)$. The spectral flows for the C_2 -symmetric twisted boundary with the symmetry center at Wyckoff positions $1a$ and $3c$ are observed in Fig. 4. The spectrum at λ and $-\lambda$ is symmetric under C_2 . Along the path $(\lambda = 1) \rightarrow (\lambda = -1)$, the irrep of spectral flow from the upper bulk bands to the lower bulk bands is A or B for a twisted boundary with the symmetry center at $1a$ or $3c$, depending on the sign of the RSIs.

When the C_6 twisted boundary is introduced into the C_{6v} system, the irreps of C_{6v} can be reduced to C_6 as

$$\begin{aligned} A_1 \downarrow 6 = A, \quad A_2 \downarrow 6 = A, \quad B_1 \downarrow 6 = B, \quad B_2 \downarrow 6 = B, \\ E_1 \downarrow 6 = {}^1E_1 \quad {}^2E_1, \quad E_2 \downarrow 6 = {}^1E_2 \quad {}^2E_2. \end{aligned} \quad (\text{A6})$$

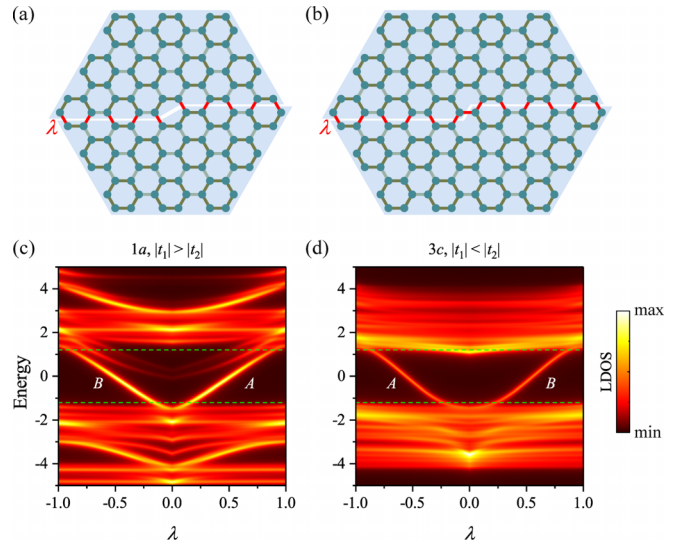


FIG. 4. (a) and (b) C_2 -symmetric twisted boundary with the symmetry center at the (b) $1a$ and (c) $3c$ maximal Wyckoff positions. The shaded regions transform into each other under rotation. The hopping strengths are multiplied by λ (red bonds) between regions. (c) and (d) Spectral flow under a C_2 -symmetric twisted boundary with the symmetry center at (c) $1a$ and (d) $3c$. The bulk band gap is between the green horizontal lines.

The reduced RSIs are $(\delta_1, \delta_2, \delta_3)_{1a} = (0, -1, -1)$ for $|t_1| > |t_2|$ and $(\delta_1, \delta_2, \delta_3)_{1a} = (0, 0, 0)$ for $|t_1| < |t_2|$. While the spectrum of the OAL($1a$) phase with $|t_1| > |t_2|$ is shown in the main text, here, we show the spectrum of the OAL($3c$) phase with $|t_1| < |t_2|$ for comparison in Fig. 5(a), where no spectral flow is present in the band gap. This topological feature is inherited in the C_5 -symmetric lattice with disclination, as shown in Fig. 5(b). The spectral flows of disclination states in the C_4 - and C_3 -symmetric lattices give similar results. By counting the imbalance in multiplicities of irreps, the RSIs describing the spectral flows in lattices with disclination are summarized in Table IV.

2. Robustness of spectral flows

We investigated the robustness of spectral flows induced by real-space topology in the C_5 -symmetric lattice by adding

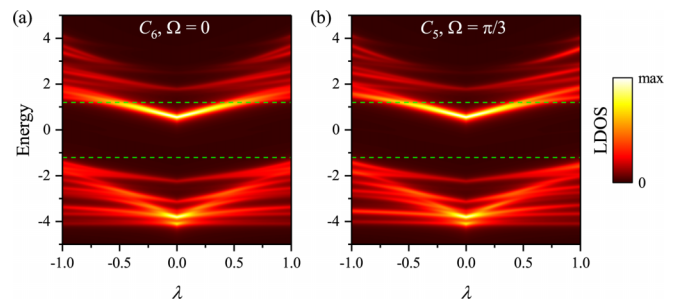


FIG. 5. Local density of states in the tight-binding model for the OAL($3c$) phase with $|t_1| < |t_2|$ as a function of the hopping multiplication factor λ . (a) C_6 -symmetric twisted boundary without a disclination. (b) C_5 -symmetric twisted boundary with a disclination of Frank angle $\pi/3$. The symmetry center of the twisted boundary is located at the $1a$ maximal Wyckoff position.

TABLE IV. Real-space invariants without spin-orbit coupling counting the imbalance in multiplicities of the irreps.

Space group	Without time-reversal symmetry	With time-reversal symmetry
2	$\delta = -m(A) + m(B)$	$\delta = -m(A) + m(B)$
3	$\delta_1 = -m(A) + m(^1E)$	$\delta = -m(A) + m(^1E \ ^2E)$
	$\delta_2 = -m(A) + m(^2E)$	
4	$\delta_1 = -m(A) + m(^1E)$	$\delta_1 = -m(A) + m(^1E \ ^2E)$
	$\delta_2 = -m(A) + m(B)$	
	$\delta_3 = -m(A) + m(^2E)$	
5	$\delta_1 = -m(A) + m(^1E_1)$	$\delta_1 = -m(A) + m(^1E_1 \ ^2E_1)$
	$\delta_2 = -m(A) + m(^1E_2)$	
	$\delta_3 = -m(A) + m(^2E_2)$	
	$\delta_4 = -m(A) + m(^2E_1)$	
6	$\delta_1 = -m(A) + m(^1E_1)$	$\delta_1 = -m(A) + m(^1E_1 \ ^2E_1)$
	$\delta_2 = -m(A) + m(^2E_2)$	
	$\delta_3 = -m(A) + m(B)$	
	$\delta_4 = -m(A) + m(^1E_2)$	
	$\delta_5 = -m(A) + m(^2E_1)$	
$6mm$	$\delta_1 = -m(A_1) - m(A_2) + m(E_1)$	$\delta_1 = -m(A_1) - m(A_2) + m(E_1)$
	$\delta_2 = -m(A_1) - m(A_2) + m(E_2)$	
	$\delta_3 = -m(A_1) - m(A_2) + m(B_1) + m(B_2)$	

a uniformly random distribution of on-site energy within an absolute value of 0.5 to lattice sites. As shown in Fig. 6, the gapless spectral flows remain robust with random on-site energy, while the disclination states may disappear at $\lambda = 1$. In Fig. 6(a), the symmetries of eigenstates are maintained while keeping the C_5 symmetry of the lattice. In Fig. 6(b), the eigenstates have no symmetry as completely random on-site energy is added, resulting in the splitting of degenerate states.

The existence of Wannier orbitals gives rise to the topological states at the disclination core. Here, we remove the core atoms of the C_6 -symmetric lattice without a disclination [Fig. 7(a)] and the C_4 -symmetric lattice with a $2\pi/3$ disclination [Fig. 7(b)]. The spectral flows and disclination states vanish in the OAL(1a) phase, as shown in Figs. 7(c) and 7(d). The removal of the core atoms induces a separation of the charge associated with the Wannier center in the OAL(3c) phase. As a result, higher-order states are observed around

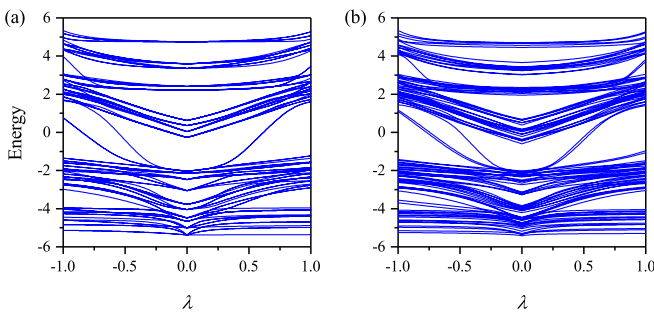


FIG. 6. Spectral flows with random on-site energy. (a) The C_5 symmetry of the lattice is maintained while adding random on-site energy. (b) Completely random on-site energy is added to the lattice sites.

the core in both lattices, as shown in Figs. 7(e) and 7(f). The spectral flows induced by the orbital of the core atoms vanish in the band gap.

We also investigated the spectral flows in lattices with negative Frank angles. The local densities of states for a C_7 -symmetric lattice with a negative Frank angle of $-\pi/3$ and a C_8 -symmetric lattice with a negative Frank angle of $-2\pi/3$ are shown in Figs. 8(a) and 8(b), respectively. The topological states behave similarly, with the disclination states having irreps of angular momentum $l = \pm 1$, while other irreps with $l \neq \pm 1$ form gapless spectral flows.

APPENDIX B: TOPOELECTRICAL CIRCUIT MODEL

1. Experiment realization in topoelectrical circuits

The behavior of an LC circuit is governed by the circuit Laplacian according to Kirchhoff's rule, $\mathbf{I}(\lambda, \omega) = J(\lambda, \omega)\mathbf{V}(\lambda, \omega)$, where \mathbf{I} denotes the current input and \mathbf{V} is the voltage against ground at each node. The components of the circuit Laplacian are analogous to the tight-binding Hamiltonian and are written as

$$J_{aa}(\lambda, \omega) = \sum_{b \neq a} i\omega C_{ab}(\lambda) - \frac{i}{\omega L_a},$$

$$J_{ab}(\lambda, \omega) = -i\omega C_{ab}(\lambda). \quad (\text{B1})$$

Here, J_{aa} and J_{ab} correspond to the on-site term and the hopping between sites, and $C_{ab}(\lambda)$ denotes the capacitors connecting different sites. We accessed the impedance Z_{ab} between two nodes a and b in experimental measurements, which is given by

$$Z_{ab} = G_{aa} + G_{bb} - G_{ab} - G_{ba}, \quad (\text{B2})$$

where $G(\lambda, \omega) = J^{-1}(\lambda, \omega)$ is the circuit Green's function. The impedance is dominated by the smallest eigenvalue

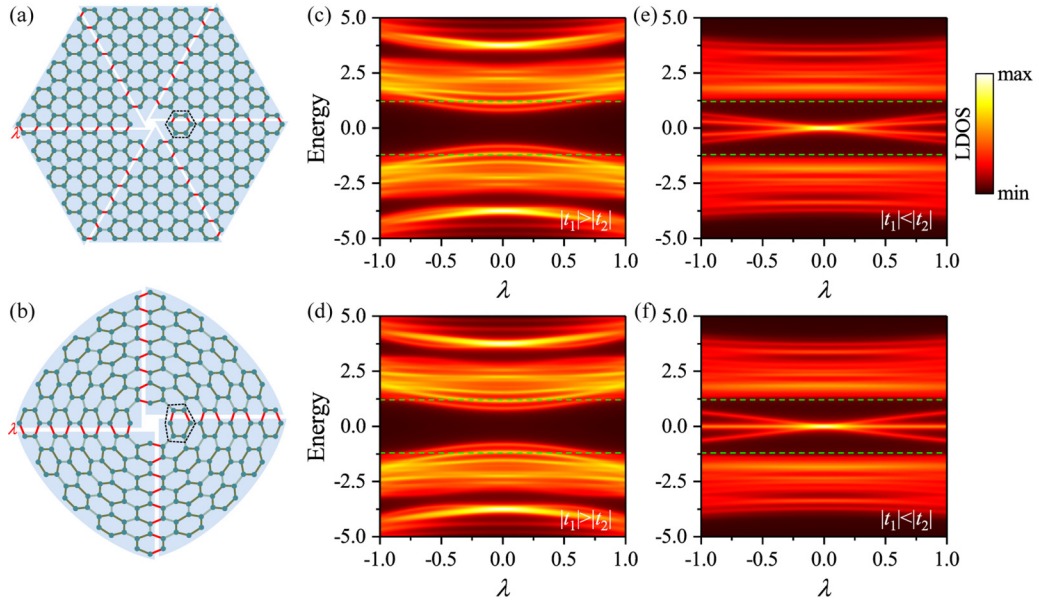


FIG. 7. Tight-binding model of (a) a C_6 -symmetric lattice without a disclination and (b) a C_4 -symmetric lattice with a $2\pi/3$ disclination. Local density of states at the unit cell in the dashed area for (c) and (d) the OAL(1a) phase with $|t_1| > |t_2|$ and (e) and (f) the OAL(3c) phase with $|t_1| < |t_2|$. We neglect the shifting of on-site energy here.

$j_n(\lambda, \omega)$ of $J(\lambda, \omega)$ at a given frequency and maps to the local density of states in the tight-binding model. In the experiment, the values of C_1 and C_2 are 2.2 and 1 nF, respectively. For hopping multiplication factors $\lambda = 0.37, 0.45$, and 1, we use capacitors of 820 pF, 1 nF, and 2.2 nF, respectively, with a tolerance of $\pm 1\%$. The on-site energy is determined by the inductors L (1 μH , $\pm 5\%$ tolerance) between the nodes and the ground, and the resonance frequency is defined as $f_0 = [2\pi\sqrt{L(2C_1 + C_2)}]^{-1}$. In the theoretical results, we applied a correction factor of 1.06 for L to account for the spurious inductive coupling between the inductors. We used a series

resistance of 450 m Ω for the inductor in simulation to fit the impedance peak observed in the experiment. We used a network analyzer (Keysight E5061B) to perform the impedance and voltage measurement.

An impedance peak appears when a zero eigenvalue exists in the admittance band structure at a given frequency. The spectrum for admittance band $j_n(\lambda, \omega)$ at frequency $1.097f_0$ is shown in Fig. 9(a), where the eigenstates of irreps 1E_2 2E_2 cross zero at $\lambda = 0.37$. For a certain hopping multiplication λ , the eigenvalues follow $j_n(\lambda, \omega) + \frac{1}{\omega L} \propto \omega$. The dispersion of $j_n(\lambda, \omega)$ with $\lambda = 0.37$ is shown in Fig. 9(b). Starting with

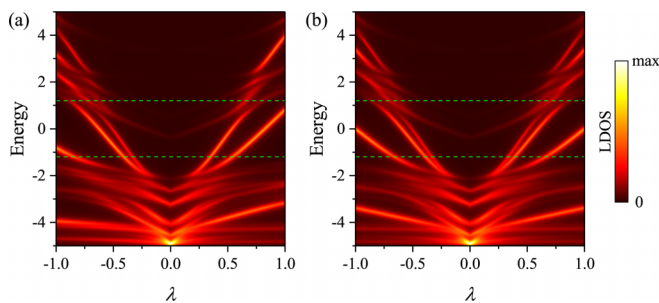


FIG. 8. Topological states and spectral flows in lattices with negative Frank angles. (a) C_7 -symmetric lattice with a Frank angle of $-\pi/3$ and (b) C_8 -symmetric lattice with a Frank angle of $-2\pi/3$.

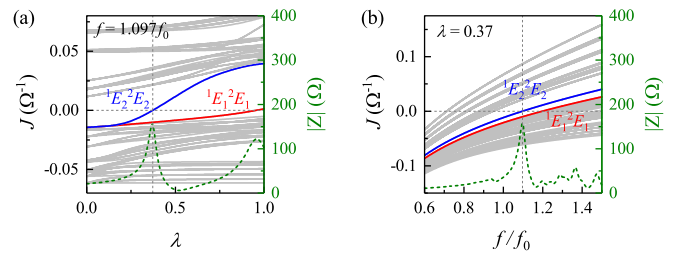


FIG. 9. (a) Theoretical spectrum of the circuit Laplacian eigenvalue of $J(\lambda, \omega)$ as a function of the hopping multiplication factor λ . The frequency is fixed at $1.097f_0$. (b) Theoretical spectrum of $J(\lambda, \omega)$ as a function of frequency at $\lambda = 0.37$. Isolate eigenvalues with small J contribute to the large impedance in the spectrum.

all $j_n(\lambda, \omega) < 0$ for small ω , the increasing frequency causes $j_n(\lambda, \omega)$ to cross zero from higher to lower bands. Therefore, the impedance bands in circuits appear upside down compared to the tight-binding model.

2. Circuit model with negative coupling

While the circuit model in the main text supports only positive λ with basic modes, here, we achieve negative λ in p -orbital bands in the circuit model. To achieve negative coupling between different sites, the phase of the signal should be inverted while propagating through the sample. Figure 10(a) shows a schematic of the C_5 -symmetric lattice, where the symmetric capacitive interconnections at twisted boundaries are twisted. The circuit Laplacian eigenvalues are composed of s - and p -orbital bands, corresponding to positive and negative λ , as shown in Fig. 10(b). The simulated impedance spectrum demonstrates the spectral flow of irrep A corresponding to negative λ while the series resistance of L is very low, as shown in Fig. 10(c). The quality factor of p -orbital bands (associated with negative λ) is significantly lower than that of s -orbital bands (associated with positive λ). Boosting the quality factor calls for circuit elements with exceptional precision and significantly reducing the resistance. However, such requirements, particularly in terms of the inductance we can source, far exceed our current experimental capabilities.

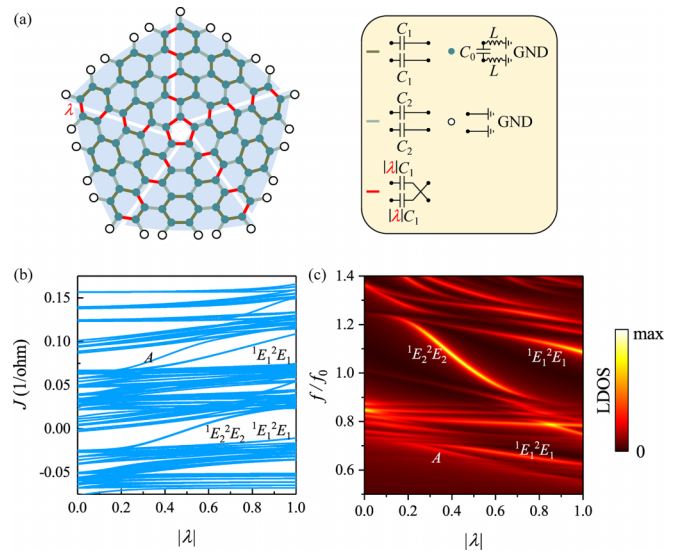


FIG. 10. (a) Circuit model of the C_5 -symmetric lattice with a disclination achieving negative λ at p -orbital bands. (b) Theoretical spectrum of the circuit Laplacian eigenvalue. (c) Simulated impedance between the ground and the node closest to the center of the electric circuit. The spectral flow of irrep A corresponds to negative λ , while 1E_2 2E_2 corresponds to positive λ . Here, C_0 is 3.3 nF, the series resistance of L is 150 m Ω , and the other parameters are the same as in the main text.

- [1] L. Ye, C. Qiu, M. Xiao, T. Li, J. Du, M. Ke, and Z. Liu, Topological dislocation modes in three-dimensional acoustic topological insulators, *Nat. Commun.* **13**, 508 (2022).
- [2] H. Xue, D. Jia, Y. Ge, Y.-J. Guan, Q. Wang, S.-Q. Yuan, H.-X. Sun, Y. D. Chong, and B. Zhang, Observation of dislocation-induced topological modes in a three-dimensional acoustic topological insulator, *Phys. Rev. Lett.* **127**, 214301 (2021).
- [3] P. Gao, D. Torrent, F. Cervera, P. San-Jose, J. Sánchez-Dehesa, and J. Christensen, Majorana-like zero modes in Kekulé distorted sonic lattices, *Phys. Rev. Lett.* **123**, 196601 (2019).
- [4] A. J. Menssen, J. Guan, D. Felce, M. J. Booth, and I. A. Walmsley, Photonic topological mode bound to a vortex, *Phys. Rev. Lett.* **125**, 117401 (2020).
- [5] J. Noh, T. Schuster, T. Iadecola, S. Huang, M. Wang, K. P. Chen, C. Chamon, and M. C. Rechtsman, Braiding photonic topological zero modes, *Nat. Phys.* **16**, 989 (2020).
- [6] W. A. Benalcazar, T. Li, and T. L. Hughes, Quantization of fractional corner charge in C_n -symmetric higher-order topological crystalline insulators, *Phys. Rev. B* **99**, 245151 (2019).
- [7] Q. Wang, H. Xue, B. Zhang, and Y. D. Chong, Observation of protected photonic edge states induced by real-space topological lattice defects, *Phys. Rev. Lett.* **124**, 243602 (2020).
- [8] Q. Wang, Y. Ge, H.-X. Sun, H. Xue, D. Jia, Y.-J. Guan, S.-Q. Yuan, B. Zhang, and Y. D. Chong, Vortex states in an acoustic Weyl crystal with a topological lattice defect, *Nat. Commun.* **12**, 3654 (2021).
- [9] B.-Y. Xie, O. You, and S. Zhang, Photonic topological pump between chiral disclination states, *Phys. Rev. A* **106**, L021502 (2022).
- [10] X.-Q. Sun, P. Zhu, and T. L. Hughes, Geometric response and disclination-induced skin effects in non-Hermitian systems, *Phys. Rev. Lett.* **127**, 066401 (2021).
- [11] C. W. Peterson, T. Li, W. Jiang, T. L. Hughes, and G. Bahl, Trapped fractional charges at bulk defects in topological insulators, *Nature (London)* **589**, 376 (2021).
- [12] Y. Liu, S. Leung, F.-F. Li, Z.-K. Lin, X. Tao, Y. Poo, and J.-H. Jiang, Bulk-disclination correspondence in topological crystalline insulators, *Nature (London)* **589**, 381 (2021).
- [13] T. Li, P. Zhu, W. A. Benalcazar, and T. L. Hughes, Fractional disclination charge in two-dimensional C_n -symmetric topological crystalline insulators, *Phys. Rev. B* **101**, 115115 (2020).
- [14] Y. Chen, Y. Yin, Z.-K. Lin, Z.-H. Zheng, Y. Liu, J. Li, J.-H. Jiang, and H. Chen, Observation of topological p -orbital disclination states in non-Euclidean acoustic metamaterials, *Phys. Rev. Lett.* **129**, 154301 (2022).
- [15] Y. Deng, W. A. Benalcazar, Z.-G. Chen, M. Oudich, G. Ma, and Y. Jing, Observation of degenerate zero-energy topological states at disclinations in an acoustic lattice, *Phys. Rev. Lett.* **128**, 174301 (2022).
- [16] Q. He, J. Sun, H.-Y. Deng, K. Wakabayashi, and F. Liu, Bound states at disclinations: An additive rule of real and reciprocal space topology, *Front. Phys.* **11**, 1213158 (2023).
- [17] B. Bradlyn, L. Elcoro, J. Cano, M. G. Vergniory, Z. Wang, C. Felser, M. I. Aroyo, and B. A. Bernevig, Topological quantum chemistry, *Nature (London)* **547**, 298 (2017).
- [18] Z.-D. Song, L. Elcoro, Y.-F. Xu, N. Regnault, and B. A. Bernevig, Fragile phases as affine monoids: Classification and material examples, *Phys. Rev. X* **10**, 031001 (2020).

- [19] L. Elcoro, B. J. Wieder, Z. Song, Y. Xu, B. Bradlyn, and B. A. Bernevig, Magnetic topological quantum chemistry, *Nat. Commun.* **12**, 5965 (2021).
- [20] J. Cano and B. Bradlyn, Band representations and topological quantum chemistry, *Annu. Rev. Condens. Matter Phys.* **12**, 225 (2021).
- [21] W. A. Benalcazar, B. A. Bernevig, and T. L. Hughes, Quantized electric multipole insulators, *Science* **357**, 61 (2017).
- [22] H. Xue, Y. Yang, F. Gao, Y. Chong, and B. Zhang, Acoustic higher-order topological insulator on a kagome lattice, *Nat. Mater.* **18**, 108 (2019).
- [23] H. C. Po, H. Watanabe, and A. Vishwanath, Fragile topology and Wannier obstructions, *Phys. Rev. Lett.* **121**, 126402 (2018).
- [24] S. Liu, A. Vishwanath, and E. Khalaf, Shift insulators: Rotation-protected two-dimensional topological crystalline insulators, *Phys. Rev. X* **9**, 031003 (2019).
- [25] Z.-D. Song, L. Elcoro, and B. A. Bernevig, Twisted bulk-boundary correspondence of fragile topology, *Science* **367**, 794 (2020).
- [26] V. Peri, Z.-D. Song, M. Serra-Garcia, P. Engeler, R. Queiroz, X. Huang, W. Deng, Z. Liu, B. A. Bernevig, and S. D. Huber, Experimental characterization of fragile topology in an acoustic metamaterial, *Science* **367**, 797 (2020).
- [27] Z.-K. Lin, Y. Wu, B. Jiang, Y. Liu, S.-Q. Wu, F. Li, and J.-H. Jiang, Topological Wannier cycles induced by sub-unit-cell artificial gauge flux in a sonic crystal, *Nat. Mater.* **21**, 430 (2022).
- [28] V. V. Albert, L. I. Glazman, and L. Jiang, Topological properties of linear circuit lattices, *Phys. Rev. Lett.* **114**, 173902 (2015).
- [29] C. H. Lee, S. Imhof, C. Berger, F. Bayer, J. Brehm, L. W. Molenkamp, T. Kiessling, and R. Thomale, Topoelectrical circuits, *Commun. Phys.* **1**, 39 (2018).
- [30] T. Hofmann, T. Helbig, C. H. Lee, M. Greiter, and R. Thomale, Chiral voltage propagation and calibration in a topoelectrical Chern circuit, *Phys. Rev. Lett.* **122**, 247702 (2019).
- [31] X.-X. Zhang and M. Franz, Non-Hermitian exceptional Landau quantization in electric circuits, *Phys. Rev. Lett.* **124**, 046401 (2020).
- [32] S. Imhof, C. Berger, F. Bayer, J. Brehm, L. W. Molenkamp, T. Kiessling, F. Schindler, C. H. Lee, M. Greiter, T. Neupert, and R. Thomale, Topoelectrical-circuit realization of topological corner modes, *Nat. Phys.* **14**, 925 (2018).
- [33] J. Noh, W. A. Benalcazar, S. Huang, M. J. Collins, K. P. Chen, T. L. Hughes, and M. C. Rechtsman, Topological protection of photonic mid-gap defect modes, *Nat. Photon.* **12**, 408 (2018).
- [34] G. van Miert and C. Ortix, Higher-order topological insulators protected by inversion and rotoinversion symmetries, *Phys. Rev. B* **98**, 081110(R) (2018).
- [35] P. Gao and J. Christensen, Topological sound pumping of zero-dimensional bound states, *Adv. Quantum Technol.* **3**, 2000065 (2020).
- [36] S. L. Altmann and P. Herzig, *Point-Group Theory Tables* (Oxford University Press, Oxford, 1994).